REVIEW

The HLLC Riemann solver

E. F. Toro[1]

Abstract

The HLLC (Harten–Lax–van Leer contact) approximate Riemann solver for computing solutions to hyperbolic systems by means of finite volume and discontinuous Galerkin methods is reviewed. HLLC was designed, as early as 1992, as an improvement to the classical HLL (Harten–Lax–van Leer) Riemann solver of Harten, Lax, and van Leer to solve systems with three or more characteristic fields, in order to avoid the excessive numerical dissipation of HLL for intermediate characteristic fields. Such numerical dissipation is particularly evident for slowly moving intermediate linear waves and for long evolution times. High-order accurate numerical methods can, to some extent, compensate for this shortcoming of HLL, but it is a costly remedy and for stationary or nearly stationary intermediate waves such compensation is very difficult to achieve in practice. It is therefore best to resolve the problem radically, at the first-order level, by choosing an appropriate numerical flux. The present paper is a review of the HLLC scheme, starting from some historical notes, going on to a description of the algorithm as applied to some typical hyperbolic systems, and ending with an overview of some of the most significant developments and applications in the last 25 years.

Keywords Hyperbolic equations · Finite volume · Discontinuous Galerkin · Numerical flux · HLLC solver · Intermediate characteristic fields · Low dissipation

1 Introduction

It is appropriate to start with some historical notes. The HLLC approximate Riemann solver is an extension of the HLL Riemann solver proposed in 1983 by Harten et al. [1]. A first version of HLLC for the time-dependent Euler equations was advanced by Toro [2]. The same year, an improved version was communicated by Toro, Spruce, and Spears as an issue of the Cranfield Technical Reports series [3] and then in 1994 as a journal paper in *Shock Waves* [4]. Also in 1994, HLLC was formulated for the steady, supersonic two-dimensional Euler equations by Toro and Chakraborty [5], where the scheme was explicitly named as HLLC. Then in 1995, Fraccarollo and Toro applied HLLC to the two-dimensional shallow water equations [6]. In 1997, some new developments were communicated by Batten et al. [7], where

analysis of the scheme was performed and new ways of estimating wave speeds were proposed. Also in 1997, Batten, Leschziner, and Goldberg proposed implicit versions of the HLLC Riemann solver, with application to turbulent flow [8].

The original HLL scheme of Harten et al. [1] computes directly an approximation to the intercell flux, only requiring estimates for the *two largest signal speeds* that bound the Riemann fan emerging from the initial discontinuity at the interface. Hence, HLL is a *two-wave model* approximate Riemann solver. Assuming that suitable estimates for the wave speeds are available, application of the integral form of the conservation laws gives a closed-form, approximate expression for the sought numerical flux. Practical HLL schemes followed after contributions from Davis [9] and Einfeldt [10], who independently proposed various ways of computing the two required wave speeds to completely determine the numerical flux. The *two-wave model* HLL approach, along with the wave speed estimates proposed by Einfeldt [10], is known as the HLLE solver. Subsequent developments on the HLL flux were reported in [11] and more recently by Dumbser and Balsara [12]. One difficulty with these various *two-wave model* schemes, however, is precisely the assumption of a *two-wave* configuration for the Riemann problem solution. The assumption is only appropriate for

✉ E. F. Toro
eleuterio.toro@unitn.it
https://eleuteriotoro.com

[1] Laboratory of Applied Mathematics, DICAM, University of Trento, Trento, Italy

hyperbolic systems of two equations, such as the conventional one-dimensional shallow water equations [13] and the one-dimensional blood flow equations [14]. For larger systems, such as the one-dimensional compressible Euler equations [15] or the split two-dimensional shallow water equations [13], the two-wave assumption carries a large error by ignoring intermediate characteristic fields. The Riemann solver becomes incomplete, in the sense that the wave model does not include all the characteristic fields present in the equations. As a consequence, the numerical resolution of physical features associated with intermediate characteristic fields, such as contact surfaces (jumps in density/entropy, jumps in concentrations), shear waves (jumps in tangential velocity components), and material interfaces, can be very inaccurate. For the limiting case in which these features are stationary relative to the mesh, the resulting numerical smearing is unacceptable.

The more accurate HLLC method reviewed here assumes a *three-wave model*. For the one-dimensional Euler equations, the three-wave model assumption is correct. It is also correct for the split three-dimensional Euler equations, as the three intermediate eigenvalues are coincident. Hence, HLLC can resolve accurately contact waves and shear waves in the transverse directions. These waves are associated with the intermediate, linearly degenerate characteristic field associated with the normal velocity. As a matter of fact, the three-wave assumption is also correct for compressible multicomponent flow with N transported species. In this case all $N + 3$ intermediate characteristic fields are coincident, and thus, HLLC can resolve entropy waves, shear waves, and all $N + 1$ contact waves. For hyperbolic systems with more than three distinct characteristic fields, the application of the HLLC idea has also been pursued in various fields; more details will be given in Sect. 7. For the 1D shallow water equations augmented by species equations for concentrations, HLLC is again applicable, as the governing equations will have three characteristic fields. An analogous situation arises with the augmented 1D blood flow equations. For the two-dimensional shallow water equations, the third intermediate characteristic field arises from the transverse velocity component, and thus, HLLC is again applicable.

The context for the present discussion is Godunov-type methods, in which the numerical flux is computed from the solution, approximate or exact, to the relevant Riemann problem. There is another class of methods that achieve upwinding in a different manner, namely flux vector splitting (FVS) methods. FVS schemes provide upwinding for fast waves at a lower computational effort and algorithm complexity than the Godunov approach with a good Riemann solver. Intermediate fields may also be well represented in the FVS approach if one adopts the more recent versions, such as that of Liou and Steffen [16]. A recent FVS scheme was proposed by Toro and Vázquez [17], which exhibits

similar performance to that of Liou and Steffen [16]; see also [18–20]. Earlier FVS schemes, such as those reported in [21–23], suffer from excessive numerical dissipation for contacts, shear waves, and shear layers. For a recent, succinct review of all major numerical fluxes for hyperbolic equations, the reader is referred to [24]; see also the textbook [15] for detailed descriptions and references.

The rest of the paper is structured as follows. Section 2 introduces the finite volume framework, the Riemann problem, and Godunov-type methods. Section 3 reviews the HLL Riemann solver of Harten et al. [1]. Sections 4–6 review the HLLC Riemann solver of Toro et al. [4,5]. Section 4 reviews HLLC for the augmented 1D shallow water equations that also includes the two-dimensional case. Section 5 describes HLLC for the augmented arterial 1D blood flow equations. Section 6 reviews HLLC for the Euler equations, including the multidimensional equations and the augmented equations for multicomponent flow. Section 7 gives an overview of developments related to HLLC in the last 25 years, from both the algorithmic and applications points of view. Conclusions are drawn in Sect. 8.

2 The finite volume method and the Riemann problem

Hyperbolic balance laws Consider the general one-dimensional (1D) system of m balance laws

$$\partial_t \mathbf{Q}(x, t) + \partial_x \mathbf{F}(\mathbf{Q}(x, t)) = \mathbf{S}(\mathbf{Q}(x, t)), \tag{1}$$

with

$$\mathbf{Q} = \begin{bmatrix} q_1 \\ q_2 \\ \cdots \\ q_m \end{bmatrix}; \quad \mathbf{F}(\mathbf{Q}) = \begin{bmatrix} f_1 \\ f_2 \\ \cdots \\ f_m \end{bmatrix}; \quad \mathbf{S}(\mathbf{Q}) = \begin{bmatrix} s_1 \\ s_2 \\ \cdots \\ s_m \end{bmatrix}. \tag{2}$$

These first-order partial differential equations are written in differential conservative form (left hand side) and admit source terms (right hand side). $\mathbf{Q}(x, t)$ is the vector of dependent variables, called *conserved variables*; $\mathbf{F}(\mathbf{Q})$ is the flux vector in the x-direction; $\mathbf{S}(\mathbf{Q})$ is the vector of source terms. Fluxes and sources are prescribed functions of $\mathbf{Q}(x, t)$. We assume system (1)–(2) to be hyperbolic, with real eigenvalues ordered as follows:

$$\lambda_1(\mathbf{Q}) \leq \lambda_2(\mathbf{Q}) \leq \lambda_3(\mathbf{Q}) \leq \cdots \leq \lambda_m(\mathbf{Q}) \tag{3}$$

and corresponding linearly independent right eigenvectors

$$\mathbf{R}_1(\mathbf{Q}), \mathbf{R}_2(\mathbf{Q}), \mathbf{R}_3(\mathbf{Q}), \ldots, \mathbf{R}_m(\mathbf{Q}). \tag{4}$$

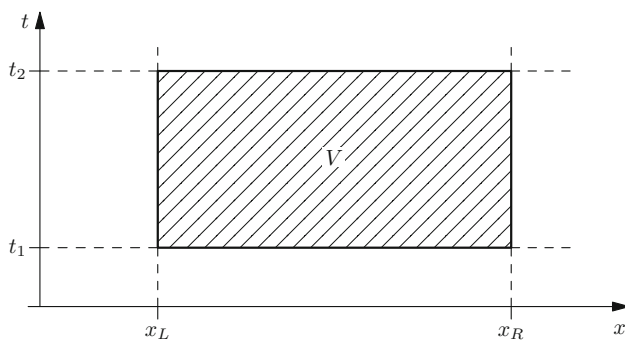This paper is concerned with numerical methods for approximating solutions to the general initial boundary value

Fig. 1 Control volume $V = [x_L, x_R] \times [t_1, t_2]$ in x–t space. The equations are integrated exactly on this control volume to derive integral forms of the conservation laws

problem (IBVP) for (1)–(2) in a domain $0 \le x \le L$ with initial conditions (ICs) and boundary conditions (BCs) given as

$$
\begin{aligned}
\text{ICs} \quad &: \quad \mathbf{Q}(x, 0) = \mathbf{Q}^{(0)}(x), \\
\text{BCs} \quad &: \quad \mathbf{Q}(0, t) = \mathbf{Q}_l(t), \quad \mathbf{Q}(L, t) = \mathbf{Q}_r(t).
\end{aligned} \tag{5}
$$

Integral forms of the equations In the presence of discontinuities, the differential form (1) is invalid, and hence, the integral form of the equations must be adopted. To this end, we consider the **control volume** $V = [x_L, x_R] \times [t_1, t_2]$ in the x–t plane, as depicted in Fig. 1. We integrate exactly equation (1) in space and time in the control volume V

$$
\begin{aligned}
\int_{x_L}^{x_R} \int_{t_1}^{t_2} [\partial_t \mathbf{Q}(x, t) &+ \partial_x \mathbf{F}(\mathbf{Q}(x, t))] \, dt \, dx \\
&= \int_{x_L}^{x_R} \int_{t_1}^{t_2} \mathbf{S}(\mathbf{Q}(x, t)) \, dt \, dx.
\end{aligned} \tag{6}
$$

On rearranging the space and time integrals, we obtain

$$
\begin{aligned}
\int_{x_L}^{x_R} & \left[\int_{t_1}^{t_2} \partial_t \mathbf{Q}(x, t) dt \right] dx \\
&= -\int_{t_1}^{t_2} \left[\int_{x_L}^{x_R} \partial_x \mathbf{F}(\mathbf{Q}(x, t)) dx \right] dt \\
&\quad + \int_{x_L}^{x_R} \int_{t_1}^{t_2} \mathbf{S}(\mathbf{Q}(x, t)) dt \, dx.
\end{aligned} \tag{7}
$$

Exact space–time integration gives the **integral form** of the balance law (1), namely

$$
\begin{aligned}
\int_{x_L}^{x_R} \mathbf{Q}(x, t_2) dx &= \int_{x_L}^{x_R} \mathbf{Q}(x, t_1) dx \\
&\quad - \left[\int_{t_1}^{t_2} \mathbf{F}(\mathbf{Q}(x_R, t)) dt - \int_{t_1}^{t_2} \mathbf{F}(\mathbf{Q}(x_L, t)) dt \right] \\
&\quad + \int_{x_L}^{x_R} \int_{t_1}^{t_2} \mathbf{S}(\mathbf{Q}(x, t)) dt \, dx.
\end{aligned} \tag{8}
$$

In the absence of the source term, the integral form states that *the amount of* $\mathbf{Q}(x, t)$ *in the interval* $[x_L, x_R]$ *at time* $t = t_2$ *is equal to the amount of* $\mathbf{Q}(x, t)$ *in the interval* $[x_L, x_R]$ *at time* $t = t_1$ *plus a difference of time integrals of the fluxes at the extreme points*. In the presence of a source term, this statement is modified appropriately.

The finite volume formula It is convenient to obtain an averaged version of (8), namely

$$
\begin{aligned}
\frac{1}{\Delta x} \int_{x_L}^{x_R} \mathbf{Q}(x, t_2) dx &= \frac{1}{\Delta x} \int_{x_L}^{x_R} \mathbf{Q}(x, t_1) dx \\
&\quad - \frac{\Delta t}{\Delta x} \left[\frac{1}{\Delta t} \int_{t_1}^{t_2} \mathbf{F}(\mathbf{Q}(x_R, t)) dt \right. \\
&\quad \left. - \frac{1}{\Delta t} \int_{t_1}^{t_2} \mathbf{F}(\mathbf{Q}(x_L, t)) dt \right] \\
&\quad + \frac{\Delta t}{\Delta x \Delta t} \int_{x_L}^{x_R} \int_{t_1}^{t_2} \mathbf{S}(\mathbf{Q}(x, t)) dt \, dx.
\end{aligned} \tag{9}
$$

The integral expression (9) can be written as

$$
\mathbf{Q}^{\text{new}} = \mathbf{Q}^{\text{old}} - \frac{\Delta t}{\Delta x} \left[\mathbf{F}_{\text{right}} - \mathbf{F}_{\text{left}} \right] + \Delta t \, \mathbf{S}_{\text{vol}}, \tag{10}
$$

which is exact, with the following definitions

$$
\begin{aligned}
\mathbf{Q}^{\text{new}} &= \frac{1}{\Delta x} \int_{x_L}^{x_R} \mathbf{Q}(x, t_2) dx, \\
\mathbf{Q}^{\text{old}} &= \frac{1}{\Delta x} \int_{x_L}^{x_R} \mathbf{Q}(x, t_1) dx, \\
\mathbf{F}_{\text{right}} &= \frac{1}{\Delta t} \int_{t_1}^{t_2} \mathbf{F}(\mathbf{Q}(x_R, t)) dt, \\
\mathbf{F}_{\text{left}} &= \frac{1}{\Delta t} \int_{t_1}^{t_2} \mathbf{F}(\mathbf{Q}(x_L, t)) dt, \\
\mathbf{S}_{\text{vol}} &= \frac{1}{\Delta x \Delta t} \int_{x_L}^{x_R} \int_{t_1}^{t_2} \mathbf{S}(\mathbf{Q}(x, t)) dt \, dx.
\end{aligned} \tag{11}
$$

Numerical methods, called *finite volume methods*, first discretise the computational domain $[0, L] \times [0, t_{\text{out}}]$ into a finite number of non-overlapping **finite volumes** as depicted in Fig. 1. Then, the *finite volume formula* (10) is used to compute approximate solutions in which $\mathbf{Q}^{\text{old}}$ is a known average of the solution at the previous time level and the remaining terms on the right hand side of (10) are found by appropriate approximations to the integrals in (11). The computational parameters Δt and Δx must be prescribed to complete the scheme to compute $\mathbf{Q}^{\text{new}}$.

In a computational setting, we assume the control volume of interest to be defined as

$$
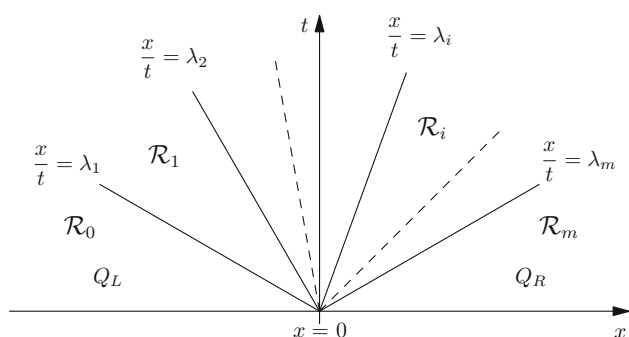V_i = \left[x_{i-\frac{1}{2}}, x_{i+\frac{1}{2}} \right] \times [t_n, t_{n+1}] \tag{12}
$$

Fig. 2 Structure of the solution to the Riemann problem for a linear system with constant coefficients. There are m waves that divide the half x–t plane into $m+1$ regions (wedges) $\mathcal{R}_i$, with $i = 0, 1, \ldots, m$. In the linear case, all waves are discontinuous and their speeds are given precisely by their associated eigenvalues (constant). In the nonlinear case, some of the waves may be smooth and wave speeds are not always given by the eigenvalues

from which the corresponding finite volume formula becomes

$$\mathbf{Q}_i^{n+1} = \mathbf{Q}_i^n - \frac{\Delta t}{\Delta x} \left[\mathbf{F}_{i+\frac{1}{2}} - \mathbf{F}_{i-\frac{1}{2}} \right] + \Delta t \mathbf{S}_i, \tag{13}$$

with the *numerical flux* $\mathbf{F}_{i+\frac{1}{2}}$ and *numerical source* $\mathbf{S}_i$ yet to be defined. From now on, we neglect the source term and concentrate on the calculation of the numerical flux.

Godunov [25] introduced the idea of computing the intercell numerical flux by approximating the time integral in (11) under the assumption that the function $\mathbf{Q}(x, t)$ under the integral is the solution to the Riemann problem in which $\mathbf{Q}_{i+\frac{1}{2}}(0)$ is the exact similarity solution $\mathbf{Q}_{i+\frac{1}{2}}(x/t)$ to the Riemann problem

$$\partial_t \mathbf{Q} + \partial_x \mathbf{F}(\mathbf{Q}) = \mathbf{0},$$
$$\mathbf{Q}(x, 0) = \begin{cases} \mathbf{Q}_L \equiv \mathbf{Q}_i^n & \text{if } x < 0, \\ \mathbf{Q}_R \equiv \mathbf{Q}_{i+1}^n & \text{if } x > 0, \end{cases} \tag{14}$$

evaluated at $x/t = 0$. Note the use of local coordinates $(\bar{x}, \bar{t})$

$$\bar{x} = x - x_{i+\frac{1}{2}}, \quad \bar{t} = t - t^n, \quad x \in [x_i, x_{i+1}],$$
$$t \in [t^n, t^{n+1}], \quad \bar{x} \in \left[-\frac{\Delta x}{2}, \frac{\Delta x}{2} \right], \quad \bar{t} \in [0, \Delta t]. \tag{15}$$

We use (x, t) to actually mean the local coordinates $(\bar{x}, \bar{t})$.

Figure 2 depicts the structure of the solution to the Riemann problem (14) for the case of a *linear* system of m equations with constant coefficients. There are m waves of speeds given by the constant eigenvalues separating $m + 1$ unknown constant regions. For a nonlinear system, the situation is analogous, but then the wave speeds are not always given by the eigenvalues and the waves are not always discontinuities. What remains true is that the solution to the Riemann problem along the t-axis is constant. That being the case, the Godunov numerical flux becomes

$$\mathbf{F}_{i+\frac{1}{2}} = \frac{1}{\Delta t} \int_{t_n}^{t_{n+1}} \mathbf{F}\left(\mathbf{Q}\left(x_{i+\frac{1}{2}}, t \right) \right) \mathrm{d}t = \mathbf{F}\left(\mathbf{Q}_{i+\frac{1}{2}}(0) \right). \tag{16}$$

That is, the Godunov flux is the *physical flux* function $\mathbf{F}(\mathbf{Q})$ of the differential equations evaluated along the volume interface $x_{i+\frac{1}{2}}$, that is along the local value $x/t = 0$; see [15], Chaps. 4 and 6 for details.

3 Review of the HLL approximate Riemann solver

In the approach of Harten et al. [1], the numerical flux $\mathbf{F}_{i+\frac{1}{2}}$ is computed directly, not as in the original Godunov's method (16) that first looks for a solution $\mathbf{Q}_{i+\frac{1}{2}}$ to the Riemann problem and then uses this to evaluate the time integral of the flux and thus the numerical flux. We first derive some integral relations that are necessary to discuss the HLL scheme.

3.1 Integral relations in the HLL approach

As in the Godunov method (16), the HLL approach considers the time integral average of the physical flux function at the volume interface introduced in (11), namely

$$\mathbf{F}_0 = \frac{1}{T} \int_0^T \mathbf{F}(\mathbf{Q}(0, t)) \mathrm{d}t \tag{17}$$

for an arbitrary time $T > 0$. Figure 3 depicts the structure of the solution to the Riemann problem (14) tailored to the HLL approach.

We first establish some useful relations obtained by applying the integral form of the conservation laws on appropriately chosen control volumes. To this end, we consider the control volume $[x_L, 0] \times [0, T]$ in the space–time configuration of Fig. 3. Assume the fastest signals perturbing the constant initial states $\mathbf{Q}_L \equiv \mathbf{Q}_i^n$ and $\mathbf{Q}_R \equiv \mathbf{Q}_{i+1}^n$ emerging from the Riemann problem solution are S_L (for left travelling signals) and S_R (for right travelling signals). Assume the wave configuration is subsonic, that is, $S_L \leq 0$ and $S_R \geq 0$. Then, for an arbitrary time $T > 0$, we define the distances

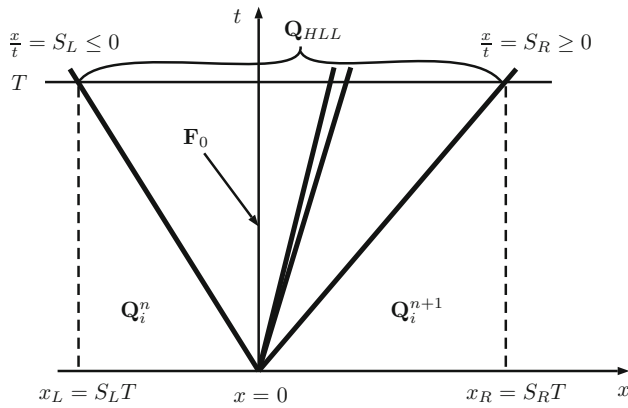$$x_L = T S_L, \quad x_R = T S_R. \tag{18}$$

Fig. 3 HLL flux. Structure of the solution to the Riemann problem tailored to the HLL approach to derive a numerical flux for the subcritical, or subsonic, cases $S_L \leq 0$ and $S_R \geq 0$. S_L and S_R represent estimates for the fastest signal speeds for the waves emerging from the break-up of the discontinuity in the Riemann problem (14)

Applying the integral form of the conservation laws (8) on the control volume $[x_L, 0] \times [0, T]$, we obtain

$$\int_{x_L}^{0} \mathbf{Q}(x, T)\mathrm{d}x = \int_{x_L}^{0} \mathbf{Q}(x, 0)\mathrm{d}x + \int_{0}^{T} \mathbf{F}(\mathbf{Q}(x_L, t))\mathrm{d}t$$
$$- \int_{0}^{T} \mathbf{F}(\mathbf{Q}(0, t))\mathrm{d}t. \qquad (19)$$

Evaluation of the first and second terms on the right hand side gives

$$\int_{x_L}^{0} \mathbf{Q}(x, 0)\mathrm{d}x = -S_L T \mathbf{Q}_L;$$
$$\int_{0}^{T} \mathbf{F}(\mathbf{Q}(x_L, t))\mathrm{d}t = T\mathbf{F}(\mathbf{Q}_L). \qquad (20)$$

Inserting these into (19), rearranging and dividing through by T gives

$$\mathbf{F}_0 = \frac{1}{T}\int_{0}^{T} \mathbf{F}(\mathbf{Q}(0, t))\mathrm{d}t$$
$$= -S_L \mathbf{Q}_L + \mathbf{F}(\mathbf{Q}_L) - \frac{1}{T}\int_{x_L}^{0} \mathbf{Q}(x, T)\mathrm{d}x. \qquad (21)$$

To completely define $\mathbf{F}_0$ approximately, it is sufficient to find an approximation to the integral on the right hand side of (21). This is what is done in the HLL approach, as seen below.

3.2 The HLL state and the HLL flux

To define $\mathbf{F}_0$ approximately, one finds an approximate state $\mathbf{Q}(x, T)$ by adopting an approach analogous to that for obtaining the Lax–Wendroff method, or the Godunov centred method; see [15]. Applying the integral form (8) of the

conservation laws (1) without a source term in the control volume $[x_L, x_R] \times [0, T]$, see Fig. 3, we obtain

$$\int_{x_L}^{x_R} \mathbf{Q}(x, T)\mathrm{d}x = \int_{x_L}^{x_R} \mathbf{Q}(x, 0)\mathrm{d}x$$
$$+ \int_{0}^{T} \mathbf{F}(\mathbf{Q}(x_L, t))\mathrm{d}t$$
$$- \int_{0}^{T} \mathbf{F}(\mathbf{Q}(x_R, t))\mathrm{d}t. \qquad (22)$$

Evaluation of the first term on the right hand side gives

$$\int_{x_L}^{x_R} \mathbf{Q}(x, 0)\mathrm{d}x = -S_L T \mathbf{Q}_L + S_R T \mathbf{Q}_R. \qquad (23)$$

Substitution of this expression into (22) and evaluation of the integrals gives

$$\int_{x_L}^{x_R} \mathbf{Q}(x, T)\mathrm{d}x = T[S_R\mathbf{Q}_R - S_L\mathbf{Q}_L + \mathbf{F}(\mathbf{Q}_L) - \mathbf{F}(\mathbf{Q}_R)]. \qquad (24)$$

On division through by $x_R - x_L = T(S_R - S_L)$, we obtain the HLL averaged state

$$\mathbf{Q}^{\mathrm{HLL}} = \frac{1}{x_R - x_L}\int_{x_L}^{x_R} \mathbf{Q}(x, T)\mathrm{d}x$$
$$= \frac{S_R\mathbf{Q}_R - S_L\mathbf{Q}_L + \mathbf{F}(\mathbf{Q}_L) - \mathbf{F}(\mathbf{Q}_R)}{S_R - S_L}. \qquad (25)$$

To complete the expression for $\mathbf{F}_0$, we now use the state $\mathbf{Q}^{\mathrm{HLL}}$ to evaluate the integral on the right hand side of (21). The resulting intercell flux is

$$\mathbf{F}_0 = \frac{S_R\mathbf{F}(\mathbf{Q}_L) - S_L\mathbf{F}(\mathbf{Q}_R) + S_L S_R(\mathbf{Q}_R - \mathbf{Q}_L)}{S_R - S_L}. \qquad (26)$$

Finally, the HLL flux for the approximate Godunov method is obtained by sampling the solution, for which the three states available are depicted in Fig. 3. The result is

$$\mathbf{F}_{i+\frac{1}{2}}^{\mathrm{HLL}} = \begin{cases} \mathbf{F}_L & \text{if } 0 \leq S_L, \\ \dfrac{S_R\mathbf{F}(\mathbf{Q}_L) - S_L\mathbf{F}(\mathbf{Q}_R) + S_L S_R(\mathbf{Q}_R - \mathbf{Q}_L)}{S_R - S_L}, & \text{if } S_L \leq 0 \leq S_R, \\ \mathbf{F}_R & \text{if } 0 \geq S_R. \end{cases} \qquad (27)$$

So far, the approach is general, as it applies to any hyperbolic system (1). The specificity comes in when providing estimates for the wave speeds S_L and S_R. We shall address this in the more general context of the HLLC Riemann solver in the following sections, for which wave speeds are provided for three specific systems of hyperbolic equations.

In the forthcoming sections, we modify the HLL scheme just described to accommodate one intermediate characteristic field following the HLLC approach. We do so for three different systems of hyperbolic equations.

4 HLLC for the shallow water equations

The HLLC Riemann solver is a modified version of the HLL solver to account for the presence of intermediate waves and was first formulated for the compressible Euler equations, the time-dependent case [3,4], and the steady supersonic case [5]. HLLC was later applied to the two-dimensional shallow water equations by Fraccarollo and Toro [6].

4.1 Equations

In this section, we review the scheme as applied to the conventional one-dimensional shallow water equations augmented with a species equation with concentration $\psi(x, t)$ transported with the normal velocity component $u(x, t)$ in the x-direction. It turns out that such a 3×3 system is formally identical to the x-split two-dimensional shallow water equations in which $\psi(x, t)$ represents the transverse velocity component v. The system contains three equations and the Riemann problem solution contains three wave families, as depicted in Fig. 4. Details of the exact solution to the Riemann problem are found in [13].

The augmented 1D shallow water equations for the case of a horizontal bottom are

$$\partial_t \mathbf{Q} + \partial_x \mathbf{F}(\mathbf{Q}) = \mathbf{0}, \tag{28}$$

with

Fig. 4 Structure of the solution to the Riemann problem for a nonlinear system of three equations in which the intermediate characteristic field is linearly degenerate. For the case of the augmented 1D shallow water equations, the intermediate wave is associated with the passive scalar $\psi(x, t)$

$$\mathbf{Q} = \begin{bmatrix} q_1 \\ q_2 \\ q_3 \end{bmatrix} = \begin{bmatrix} h \\ hu \\ h\psi \end{bmatrix},$$

$$\mathbf{F}(\mathbf{Q}) = \begin{bmatrix} f_1 \\ f_2 \\ f_3 \end{bmatrix} = \begin{bmatrix} hu \\ hu^2 + \frac{1}{2}gh^2 \\ h\psi u \end{bmatrix}. \tag{29}$$

$\mathbf{Q}$ is the vector of conserved variables and $\mathbf{F}(\mathbf{Q})$ is the physical flux vector. Here, $h(x, t)$ is the flow depth, $u(x, t)$ is the velocity, $\psi(x, t)$ is the concentration of a species transported with velocity u, and g is a parameter of the problem and represents the acceleration due to gravity, taken here as $g = 9.81$ m/s^2. The system has three real eigenvalues

$$\lambda_1 = u - a, \quad \lambda_2 = u, \quad \lambda_3 = u + a, \tag{30}$$

where $a = \sqrt{gh}$ is the *celerity*. Figure 4 depicts the structure of the solution to the Riemann problem, with three wave families. The intermediate wave associated with the intermediate eigenvalue $\lambda_2 = u$ is a linearly degenerate field, and this in turn is associated with the passive scalar $\psi(x, t)$. The outer waves corresponding to the eigenvalues $\lambda_1 = u - a$ and $\lambda_3 = u + a$ define genuinely nonlinear waves and are associated with either rarefaction waves or shock waves (bores) [13].

4.2 Derivation of the HLLC flux

To derive the HLLC flux, we consider the wave pattern depicted in Fig. 5, where a generic intermediate wave of speed S_* is present. Application of the integral form (8) of the conservation laws without source term in $[x_L, 0] \times [0, T]$ and in $[0, x_R] \times [0, T]$ yields, respectively,

$$\mathbf{F}_{*L} = \mathbf{F}_L + S_L(\mathbf{Q}_{*L} - \mathbf{Q}_L), \quad \mathbf{F}_{*R} = \mathbf{F}_R + S_R(\mathbf{Q}_{*R} - \mathbf{Q}_R). \tag{31}$$

Here, there are two vector equations for the four unknown vectors $\mathbf{Q}_{*L}, \mathbf{Q}_{*R}, \mathbf{F}_{*L}$, and $\mathbf{F}_{*R}$ in the star region, see Fig. 5. To solve this underdetermined algebraic system, we make the following additional assumptions

$$h_{*L} = h_{*R} = h_*, \quad u_{*L} = u_{*R} = u_* = S_*. \tag{32}$$

As a matter of fact, the above assumptions are true for the exact Riemann solver, see [13,26]. From the first component of the first vector equation in (31), we write

$$h_* u_* = h_L u_L + S_L(h_* - h_L). \tag{33}$$

From the first component of the second vector equation in (31), we obtain

$$h_* u_* = h_R u_R + S_R(h_* - h_R). \tag{34}$$

From (33) and (34), we have

$$h_* = \frac{h_R(u_R - S_R)}{u_* - S_R} = \frac{h_L(u_L - S_L)}{u_* - S_L}. \tag{35}$$

From here, we obtain an estimate for the intermediate wave speed S_* in terms of assumed outer wave speed estimates S_L and S_R, namely

$$S_* \equiv u_* = \frac{S_L h_R(u_R - S_R) - S_R h_L(u_L - S_L)}{h_R(u_R - S_R) - h_L(u_L - S_L)}. \tag{36}$$

Once S_L and S_R are known, h_* is known from (35)–(36). Then, the vectors $\mathbf{Q}_{*L}$ and $\mathbf{Q}_{*R}$ in (31) are given as

$$\mathbf{Q}_{*L} = h_* \begin{bmatrix} 1 \\ S_* \\ \psi_L \end{bmatrix}, \quad \mathbf{Q}_{*R} = h_* \begin{bmatrix} 1 \\ S_* \\ \psi_R \end{bmatrix}. \tag{37}$$

Now the vectors $\mathbf{F}_{*L}$ and $\mathbf{F}_{*R}$ in (31) are determined, and finally, the HLLC flux is sampled in the four regions depicted in Fig. 5, to obtain

$$\mathbf{F}_{i+\frac{1}{2}}^{\mathrm{HLLC}} = \begin{cases} \mathbf{F}_L & \text{if } 0 \le S_L, \\[2mm] \mathbf{F}_{*L} = \mathbf{F}_L + S_L(\mathbf{Q}_{*L} - \mathbf{Q}_L) & \text{if } S_L \le 0 \le S_*, \\[2mm] \mathbf{F}_{*R} = \mathbf{F}_R + S_R(\mathbf{Q}_{*R} - \mathbf{Q}_R) & \text{if } S_* \le 0 \le S_R, \\[2mm] \mathbf{F}_R & \text{if } 0 \ge S_R, \end{cases} \tag{38}$$
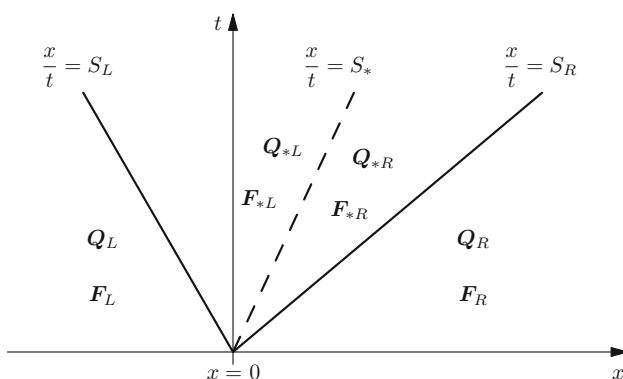
Fig. 5 Assumed wave pattern for the HLLC Riemann solver. The star region contains two sub-regions separated by the intermediate wave. This wave structure represents precisely the exact solution to the Riemann problem for the shallow water equations. This pattern is also valid for the 3D Euler equations in which the middle eigenvalue is repeated

where the states $\mathbf{Q}_{*L}, \mathbf{Q}_{*R}$ are given by (37). To complete the description of the HLLC scheme, it is necessary to provide estimates for the outer wave speeds S_L and S_R, which is done below.

4.3 Wave speed estimates

Following [13], the following estimates S_L and S_R for the outer wave speeds are suggested

$$S_L = u_L - q_L a_L, \quad S_R = u_R + q_R a_R, \tag{39}$$

where q_K ($K = L, R$) are obtained according to the type of nonlinear waves present in the system. In [13], the following expressions are proposed

$$q_K = \begin{cases} \sqrt{\dfrac{1}{2} \dfrac{(\bar{h}_* + h_K)\bar{h}_*}{h_K^2}} & \text{if } \bar{h}_* > h_K, \quad \text{shock wave}, \\[4mm] 1 & \text{if } \bar{h}_* \le h_K, \quad \text{rarefaction wave}. \end{cases} \tag{40}$$

Here, $\bar{h}_*$ is an approximation to the exact value h_* in the star region for which there are various possible choices. Here, we suggest using simple but robust estimate

$$\bar{h}_* = \frac{a_{\mathrm{TR}}^2}{g}, \quad a_{\mathrm{TR}} = \frac{1}{2}(a_L + a_R) - \frac{1}{4}(u_R - u_L). \tag{41}$$

Here, a_{TR} is an estimate for the celerity a based on the assumption that the two outer nonlinear waves are rarefaction waves; see [13] for details.

4.4 HLLC algorithm for shallow water

To implement HLLC to solve the shallow water equations (augmented or the two-dimensional equations), the following sequence of steps are performed:

1. $\bar{h}_*$ is computed from (41).
2. q_K ($K = L, R$) are computed from (40).
3. S_L and S_L are computed from (39), and S_* is computed from (36).
4. $\mathbf{Q}_{*L}$ and $\mathbf{Q}_{*R}$ are computed from (37).
5. $\mathbf{F}_{*L}$ or $\mathbf{F}_{*R}$ are computed from (38), according to the wave pattern, and the HLLC flux follows.

The HLLC numerical flux for shallow water has been determined. We remark that in the absence of the species equation for ψ, the classical 2×2 one-dimensional system of equations in (42) is recovered; the simpler HLL flux described in Sect. 3 is then applicable. For the two-dimensional shallow water equations, the derivations performed earlier including ψ are applicable, in which ψ is identical to the transverse

velocity component. If species advection equations are added to the conventional 2D shallow water equations, then the procedure to derive the corresponding HLLC flux is analogous to that just described, see [13] for details.

5 The HLLC flux for the equations of blood flow in arteries

Computational methods for medical fluid dynamics, for blood flow in arteries or veins for example, are beginning to make significant progress [27]. Here, we restrict our attention to blood flow in arteries. For the more challenging case of veins see [28,29], and the review [14] and references therein.

5.1 Governing equations

The cross-section averaged equations for the flow of blood in a single arterial vessel, along with a species transport equation with associated concentration $\psi(x, t)$, are

$$
\begin{aligned}
&\partial_t A + \partial_x (uA) = 0, \\
&\partial_t (uA) + \partial_x (\hat{\alpha} A u^2) + \frac{A}{\rho} \partial_x p = -R u, \\
&\partial_t \psi + u \partial_x \psi = 0.
\end{aligned}
\tag{42}
$$

$A(x, t)$ is the cross-sectional area of the vessel at position x and time t; $u(x, t)$ is the averaged velocity of blood at a cross section; $p(x, t)$ is pressure; $R > 0$ is the viscous resistance, a prescribed function; ρ is blood density, assumed constant; and $\hat{\alpha}$ is the Coriolis coefficient that depends on the assumed velocity profile. There are three unknowns and two equations, and thus, a closure condition, called *tube law*, is needed to close the system. A purely elastic tube law for arteries takes the form

$$
p = p_{\text{ext}}(x, t) + \beta(x)\phi(A)
\tag{43}
$$

with

$$
\phi(A) = \sqrt{A} - \sqrt{A_0}, \quad \beta(x) = \frac{\sqrt{\pi}}{1 - \nu^2} \cdot \frac{h_0(x)E(x)}{A_0(x)}. \tag{44}
$$

Here,

$$
p_{\text{trans}} \equiv \beta \phi(A) = p - p_{\text{ext}}
\tag{45}
$$

is the *transmural pressure*. The tube law involves geometrical and mechanical parameters, assumed to be prescribed. $A_0(x)$ is the equilibrium cross-sectional area; $h_0(x)$ is the vessel wall thickness; $E(x)$ is the Young's modulus of elasticity; and ν is the Poisson ratio, taken as $\nu = 1/2$. For veins, a different tube law is used.

From now on, we assume that h_0, A_0, E, and p_{ext} are constant. We also assume $\hat{\alpha} = 1$. Therefore, $\beta(x)$ in (44) is constant and the non-conservative term $\frac{A}{\rho}\partial_x p$ in (42) becomes $\frac{A}{\rho}\partial_x p = \gamma \partial_x A^{3/2}$ with

$$
\gamma = \frac{\beta}{3\rho} = \frac{1}{3\rho} \cdot \frac{\sqrt{\pi}}{1 - \nu^2} \cdot \frac{h_0(x)E(x)}{A_0(x)}.
\tag{46}
$$

Thus, the momentum equation can be expressed in conservation-law form. Also the third equation in (42) can be expressed in conservation form by combining it with the continuity equation. Therefore, in differential form, now the principal part of the full system (42) can be written in conservation-law form, giving rise to the system of balance laws

$$
\partial_t \mathbf{Q} + \partial_x \mathbf{F}(\mathbf{Q}) = \mathbf{S}(\mathbf{Q}),
\tag{47}
$$

where

$$
\begin{aligned}
\mathbf{Q} &= \begin{bmatrix} q_1 \\ q_2 \\ q_3 \end{bmatrix} \equiv \begin{bmatrix} A \\ Au \\ A\psi \end{bmatrix}, \\
\mathbf{F}(\mathbf{Q}) &= \begin{bmatrix} f_1 \\ f_2 \\ f_3 \end{bmatrix} \equiv \begin{bmatrix} Au \\ Au^2 + \gamma A^{3/2} \\ Au\psi \end{bmatrix}, \\
\mathbf{S}(\mathbf{Q}) &= \begin{bmatrix} s_1 \\ s_2 \\ s_3 \end{bmatrix} \equiv \begin{bmatrix} 0 \\ -Ru \\ 0 \end{bmatrix}.
\end{aligned}
\tag{48}
$$

We remark that equations (42) can still be written in conservation-law form for the case of variable material properties. The principal part of (48), when written in quasi-linear form, becomes

$$
\partial_t \mathbf{Q} + \mathbf{A}(\mathbf{Q})\partial_x \mathbf{Q} = \mathbf{0},
\tag{49}
$$

with the Jacobian matrix given as

$$
\mathbf{A}(\mathbf{Q}) = \begin{bmatrix} 0 & 1 & 0 \\ \frac{3}{2}\gamma\sqrt{A} - u^2 & 2u & 0 \\ -u\psi & \psi & u \end{bmatrix}.
\tag{50}
$$

The eigenvalues of (49) are all real and are given by

$$
\lambda_1 = u - c, \quad \lambda_2 = u, \quad \lambda_3 = u + c,
\tag{51}
$$

where c is the *wave speed* given as

$$
c = \sqrt{\frac{3}{2}\gamma\sqrt{A}}.
\tag{52}
$$

The right eigenvectors of $\mathbf{A}$ corresponding to the eigenvalues (51) are

$$\mathbf{R}_1 = \beta_1 \begin{bmatrix} 1 \\ u - c \\ \psi \end{bmatrix}, \quad \mathbf{R}_2 = \beta_2 \begin{bmatrix} 0 \\ 0 \\ 1 \end{bmatrix},$$

$$\mathbf{R}_3 = \beta_3 \begin{bmatrix} 1 \\ u + c \\ \psi \end{bmatrix}, \tag{53}$$

where β_1, β_2, and β_3 are arbitrary scaling factors. For further details on the equations and the exact solution to the Riemann problem, see [14].

5.2 Derivation of the HLLC Riemann solver for blood flow

Here, we derive the HLLC flux for the augmented blood flow equations (47)–(48). Note that in the absence of the species equation for ψ, the classical 2×2 system of equations in (42) is obtained, and the simpler HLL flux of Sect. 3 applies directly. To construct the intercell numerical flux at each cell interface, we consider the local Riemann problem

$$\partial_t \mathbf{Q} + \partial_x \mathbf{F}(\mathbf{Q}) = \mathbf{0},$$
$$\mathbf{Q}(x, 0) = \begin{cases} \mathbf{Q}_L \equiv \mathbf{Q}_i^n & \text{if } x < 0, \\[2mm] \mathbf{Q}_R \equiv \mathbf{Q}_{i+1}^n & \text{if } x > 0. \end{cases} \tag{54}$$

The structure of the exact solution is as depicted in Fig. 4, see [14] for details. For the purpose of deriving HLLC, let us consider the wave pattern depicted in Fig. 5, where an intermediate wave of speed S_* is present. Application of the integral form of the conservation laws (8) without source term in $[x_L, 0] \times [0, T]$ and in $[0, x_R] \times [0, T]$, with $T > 0$, yields

$$\mathbf{F}_{*L} = \mathbf{F}_L + S_L(\mathbf{Q}_{*L} - \mathbf{Q}_L),$$
$$\mathbf{F}_{*R} = \mathbf{F}_R + S_R(\mathbf{Q}_{*R} - \mathbf{Q}_R), \tag{55}$$

where the four vectors $\mathbf{Q}_{*L}$, $\mathbf{Q}_{*R}$, $\mathbf{F}_{*L}$, and $\mathbf{F}_{*R}$ are unknown. To solve this underdetermined algebraic problem, we make the following assumptions

$$A_{*L} = A_{*R} = A_*, \quad u_{*L} = u_{*R} = u_* = S_*. \tag{56}$$

As a matter of fact, these assumptions are satisfied by the exact solution to the Riemann problem [14]. From the first component of the first vector equation in (55), we write

$$A_* u_* = A_L u_L + S_L(A_* - A_L). \tag{57}$$

From the first component of the second vector equation in (55), we write

$$A_* u_* = A_R u_R + S_R(A_* - A_R). \tag{58}$$

From (57) and (58), we have

$$A_* = \frac{A_R(u_R - S_R)}{u_* - S_R} = \frac{A_L(u_L - S_L)}{u_* - S_L}, \tag{59}$$

and from here, we obtain

$$S_* \equiv u_* = \frac{S_L A_R(u_R - S_R) - S_R A_L(u_L - S_L)}{A_R(u_R - S_R) - A_L(u_L - S_L)}. \tag{60}$$

If S_L and S_R have been prescribed, then A_* and u_* are known from (59)–(60), and the vectors $\mathbf{Q}_{*L}$ and $\mathbf{Q}_{*R}$ in (55) are given as

$$\mathbf{Q}_{*L} = A_* \begin{bmatrix} 1 \\ S_* \\ \psi_L \end{bmatrix}, \quad \mathbf{Q}_{*R} = A_* \begin{bmatrix} 1 \\ S_* \\ \psi_R \end{bmatrix}. \tag{61}$$

Now the vectors $\mathbf{F}_{*L}$ and $\mathbf{F}_{*R}$ in (55) are determined. Finally, the HLLC flux is identical in form to that derived for shallow water, which we repeat here as

$$\mathbf{F}_{i+\frac{1}{2}}^{\text{HLLC}} = \begin{cases} \mathbf{F}_L & \text{if } 0 \leq S_L, \\[2mm] \mathbf{F}_{*L} = \mathbf{F}_L + S_L(\mathbf{Q}_{*L} - \mathbf{Q}_L) & \text{if } S_L \leq 0 \leq S_*, \\[2mm] \mathbf{F}_{*R} = \mathbf{F}_R + S_R(\mathbf{Q}_{*R} - \mathbf{Q}_R) & \text{if } S_* \leq 0 \leq S_R, \\[2mm] \mathbf{F}_R & \text{if } 0 \geq S_R, \end{cases} \tag{62}$$

where the states $\mathbf{Q}_{*L}$ and $\mathbf{Q}_{*R}$ are given by (61).

5.3 Wave speed estimates for HLLC

Assume an estimate $\bar{A}_*$ for A^* as follows:

$$\bar{A}_* = \frac{4\bar{c}_*^4}{9\gamma^2}, \quad \text{with} \quad \bar{c}_* = \frac{1}{2}(c_L + c_R) - \frac{1}{8}(u_R - u_L). \tag{63}$$

Here $\bar{c}_*$ is an approximation to the wave speed obtained from assuming a two-rarefaction wave pattern in the exact Riemann problem solution [14]. From here, we compute the parameter

$$M_K = \sqrt{\frac{\gamma A_K \bar{A}_* (\bar{A}_*^{3/2} - A_K^{3/2})}{\bar{A}_* - A_K}}, \quad K = L, R. \tag{64}$$

Then, the outer wave speeds are calculated as follows:

$$S_L = \begin{cases} u_L - c_L & \text{if } \bar{A}_* \leq A_L \quad \text{(Left rarefaction)} \\ \\ u_L - M_L/A_L & \text{if } \bar{A}_* > A_L \quad \text{(Left shock)} \end{cases} \tag{65}$$

$$S_R = \begin{cases} u_R + c_R & \text{if } \bar{A}_* \leq A_R \quad \text{(Right rarefaction)} \\ \\ u_R + M_R/A_R & \text{if } \bar{A}_* > A_R \quad \text{(Right shock)} \end{cases} \tag{66}$$

Once S_L and S_R have been obtained from (65)–(66), the intermediate wave speed is calculated as in (60).

5.4 HLLC algorithm for blood flow in arteries

To implement HLLC to solve the augmented 1D blood flow equations for arteries, the following sequence of steps are performed:

1. $\bar{A}_*$ is computed from (63).
2. M_K ($K = L, R$) are computed from (64).
3. S_L and S_R are computed from (65)–(66), and S_* is computed from (60).
4. $\mathbf{Q}_{*L}$ and $\mathbf{Q}_{*R}$ are computed from (61).
5. $\mathbf{F}_{*L}$ or $\mathbf{F}_{*R}$ are computed from (62), according to the wave pattern, and the HLLC flux is thus known.

The complete HLLC numerical flux for the augmented blood flow equations for arteries is then determined.

6 HLLC for compressible gas dynamics

The HLLC Riemann solver was actually first put forward for the compressible Euler equations of gas dynamics by Toro et al. [3–5]. For subsequent, early developments, see [7,8]. For the Euler equations, the need to account for intermediate characteristic fields was made obvious by the *contact discontinuity* in the time-dependent one-dimensional case [3,4] and hence the name HLLC, where "C" accounts for *contact*. In the steady supersonic two-dimensional case [5], it was the *slip surface* that motivated the introduction of HLLC. For the multidimensional, time-dependent case, the presence of *shear waves* in the transverse directions reinforces the need to account for additional intermediate characteristic fields when designing the numerical flux. The acknowledgement of such fields has strong implications also for solving the compressible Navier–Stokes equations, in resolving vortical flows and shear layers accurately.

6.1 The Euler equations

The three-dimensional Euler equations read

$$\partial_t \mathbf{Q} + \partial_x \mathbf{F}(\mathbf{Q}) + \partial_y \mathbf{G}(\mathbf{Q}) + \partial_z \mathbf{H}(\mathbf{Q}) = \mathbf{0}, \tag{67}$$

where the vector of unknowns $\mathbf{Q}$ and physical fluxes are

$$\begin{aligned} \mathbf{Q} &= [\rho, \rho u, \rho v, \rho w, E]^{\mathrm{T}}, \\ \mathbf{F}(\mathbf{Q}) &= \left[\rho u, \rho u^2 + p, \rho u v, \rho u w, u(E + p)\right]^{\mathrm{T}}, \\ \mathbf{G}(\mathbf{Q}) &= \left[\rho v, \rho u v, \rho v^2 + p, \rho v w, v(E + p)\right]^{\mathrm{T}}, \\ \mathbf{H}(\mathbf{Q}) &= \left[\rho w, \rho u w, \rho v w, \rho w^2 + p, w(E + p)\right]^{\mathrm{T}}. \end{aligned} \tag{68}$$

Full details are found in [15]. Here, ρ is density; u, v, and w are particle velocity components in the x-, y-, and z-directions, respectively; p is pressure and E is total energy given in terms of specific kinetic energy $V^2/2 = (u^2 + v^2 + w^2)/2$ and specific internal energy e as

$$E = \rho \left(\frac{1}{2} V^2 + e\right), \quad e(\rho, p) = \frac{p}{\rho(\gamma - 1)}. \tag{69}$$

The function $e = e(\rho, p)$ is called the (caloric) *equation of state*. Here, we have taken the ideal gas case, where $1 < \gamma < 5/3$ is the ratio of specific heats, a constant. For air at moderate pressures and temperatures, one uses $\gamma = 1.4$.

For the purpose of determining a numerical flux for the three-dimensional Euler equations that is normal to a cell interface, by virtue of the rotational invariance, it is sufficient to consider the augmented one-dimensional Euler equations aligned in that normal direction. Here, without loss of generality, we assume the normal direction to be the x-direction. The equations of interest are therefore

$$\partial_t \mathbf{Q} + \partial_x \mathbf{F}(\mathbf{Q}) = \mathbf{0}, \tag{70}$$

with $\mathbf{Q}$ and $\mathbf{F}(\mathbf{Q})$ as in (67)–(68). The associated 5×5 Jacobian matrix has eigenvalues

$$\lambda_1(\mathbf{Q}) = u - a, \quad \lambda_2(\mathbf{Q}) = \lambda_3(\mathbf{Q}) = \lambda_4(\mathbf{Q}) = u, \\ \lambda_5(\mathbf{Q}) = u + a, \tag{71}$$

where a is the *speed of sound*, given as

$$a = \sqrt{\frac{\gamma p}{\rho}}. \tag{72}$$

For a full description of the HLLC method as applied to the compressible three-dimensional Euler equations, the reader is referred to the textbook [15].

Here, we review the current version of HLLC as applied to the three-dimensional ideal Euler equations (67)–(68), extended to include N species equations for N concentrations ψ_i. Now the vector $\mathbf{Q}$ of conserved variables and the flux in the x-direction are

$$\mathbf{Q} = [\rho, \rho u, \rho v, \rho w, E, \rho \psi_1, \ldots, \rho \psi_N]^{\mathrm{T}},$$
$$\mathbf{F}(\mathbf{Q}) = \left[\rho u, \rho u^2 + p, \rho u v, \rho u w, u(E + p), \rho u \psi_1, \ldots, \rho u \psi_N\right]^{\mathrm{T}}.$$
(73)

The associated $(5 + N) \times (5 + N)$ Jacobian matrix has eigenvalues

$$\lambda_1(\mathbf{Q}) = u - a, \quad \lambda_2(\mathbf{Q}) = \lambda_3(\mathbf{Q}) = \cdots = \lambda_{4+N}(\mathbf{Q}) = u,$$
$$\lambda_{5+N}(\mathbf{Q}) = u + a.$$
(74)

Note that the intermediate eigenvalue $\lambda_2(\mathbf{Q}) = u$ has multiplicity $N + 3$. It can be shown that a complete set of linearly independent eigenvectors corresponding to the real eigenvalues (74) exists, and therefore, the problem is hyperbolic, even if not strictly hyperbolic.

6.2 HLLC flux for the Euler equations

At each cell interface, we consider the local Riemann problem

$$\partial_t \mathbf{Q} + \partial_x \mathbf{F}(\mathbf{Q}) = \mathbf{0},$$
$$\mathbf{Q}(x, 0) = \begin{cases} \mathbf{Q}_L \equiv \mathbf{Q}_i^n & \text{if } x < 0, \\ \mathbf{Q}_R \equiv \mathbf{Q}_{i+1}^n & \text{if } x > 0. \end{cases}$$
(75)

The structure of the exact solution is analogous to that depicted in Fig. 4, with the two outer waves representing the wave families associated with the eigenvalues $\lambda_1(\mathbf{Q})$ and $\lambda_{5+N}(\mathbf{Q})$, respectively. The middle wave accounts for the remaining characteristic fields. For the purpose of deriving the HLLC flux, we refer to Fig. 5. Note that for the x-split 3D multicomponent Euler equations, the middle eigenvalue has multiplicity $N + 3$, where N is the total number of species equations. Therefore, by restoring the contact discontinuity associated with the entropy wave, we also restore two shear waves and the N contact discontinuities associated with the N concentrations ψ_k.

First, we assume that wave speed estimates S_L, S_*, and S_R for the three wave families depicted in Fig. 5 are available. Then, by integrating in appropriate control volumes around the waves of speeds S_L and S_R we obtain averaged-type Rankine–Hugoniot conditions

$$\mathbf{F}_{*L} = \mathbf{F}_L + S_L(\mathbf{Q}_{*L} - \mathbf{Q}_L),$$
$$\mathbf{F}_{*R} = \mathbf{F}_R + S_R(\mathbf{Q}_{*R} - \mathbf{Q}_R),$$
(76)

with

$$\mathbf{Q}_{*K} = [\rho_{*K}, \rho_{*K} u_*, \rho_{*K} v_K, \rho_{*K} w_K, E_{*K}, \rho_{*K} \psi_1, \ldots, \rho_{*K} \psi_N]^{\mathrm{T}},$$
$$K = L \text{ or } K = R.$$
(77)

This gives rise to a large, underdetermined algebraic system with more unknowns than equations. One way to resolve this difficulty is to introduce a number of assumptions, all consistent with the exact solution to the Riemann problem (75), leading to the following expressions for the intermediate state vectors in (76)

$$\mathbf{Q}_{*K} = \rho_K \left(\frac{S_K - u_K}{S_K - S_*}\right) \begin{bmatrix} 1 \\ S_* \\ v_K \\ w_K \\ \frac{E_K}{\rho_K} + (S_* - u_K)\left[S_* + \frac{p_K}{\rho_K(S_K - u_K)}\right] \\ (q_1)_K \\ \cdots \\ (q_l)_K \\ \cdots \\ (q_N)_K \end{bmatrix},$$
(78)

$K = L$ or $K = R$. Then, the intermediate fluxes $\mathbf{F}_{*L}$ and $\mathbf{F}_{*R}$ in (76) are completely determined and the numerical flux is then given as

$$\mathbf{F}_{i+\frac{1}{2}}^{\mathrm{HLLC}} = \begin{cases} \mathbf{F}_L & \text{if } 0 \le S_L, \\ \mathbf{F}_{*L} & \text{if } S_L \le 0 \le S_*, \\ \mathbf{F}_{*R} & \text{if } S_* \le 0 \le S_R, \\ \mathbf{F}_R & \text{if } 0 \ge S_R. \end{cases}$$
(79)

The missing items for implementing both HLL and HLLC are the wave speed estimates.

6.3 Wave speed estimates for HLLC

For HLL, having a two-wave model, we only need estimates for S_L and S_R. The following choice [15] has proved useful

$$S_L = u_L - a_L q_L, \quad S_R = u_R + a_R q_R,$$
(80)

with

$$q_K = \begin{cases} 1 & \text{if } \bar{p}_* \le p_K, \\ \left[1 + \frac{\gamma + 1}{2\gamma}\left(\frac{\bar{p}_*}{p_K} - 1\right)\right]^{1/2} & \text{if } \bar{p}_* > p_K, \end{cases}$$
(81)

where $\bar{p}_*$ is an estimate for the pressure p_* in the star region, see Fig. 5. Note that in (81) one discriminates between rar-

efactions and shocks. Regarding $\bar{p}_*$ in (81), a very reliable choice is the two-rarefaction approximation

$$\bar{p}_* = \left[\frac{a_L + a_R - \frac{\gamma-1}{2}(u_R - u_L)}{a_L/p_L^z + a_R/p_R^z} \right]^{1/z}, \quad z = \frac{\gamma - 1}{2\gamma}. \quad (82)$$

This approximation is obtained by assuming *a priori* that the two pressure waves (the fastest waves in the Riemann problem solution) are rarefaction waves, see [15] for details. For the HLLC solver, we need additionally the intermediate speed S_*. This can be found in terms of S_L and S_R as

$$S_* = \frac{p_R - p_L + \rho_L u_L(S_L - u_L) - \rho_R u_R(S_R - u_R)}{\rho_L(S_L - u_L) - \rho_R(S_R - u_R)}. \quad (83)$$

Generally, the proposed wave speed estimates have been found to be very robust, over the years. However, there are extreme situations in which care is required, as pointed out by Safranov [30].

6.4 HLLC algorithm for the Euler equations

To implement HLLC to solve the augmented 3D Euler equations, the following steps are performed in sequence:

1. $\bar{p}_*$ is computed from (82).
2. q_L and q_R are computed from (81).
3. S_L and S_R are computed from (80), and S_* is computed from (83).
4. $\mathbf{Q}_{*L}$ and $\mathbf{Q}_{*R}$ are computed from (78).
5. $\mathbf{F}_{*L}$ or $\mathbf{F}_{*R}$ are computed from (79), according to the wave pattern, and thus, the HLLC flux is known.

The complete HLLC numerical flux for the three-dimensional Euler equations for multicomponent flow with N species has been determined.

6.5 Performance of HLLC as compared to HLL

A crucial difference between HLL and HLLC is seen in the resolution of contact discontinuities and shear waves, with larger differences occurring for slowly moving intermediate waves. The extreme case is the stationary wave. To illustrate this point, we solve the one-dimensional Euler equations in the domain $0 \le x \le 1$ with initial conditions $\rho(x, 0) = 1.4$ for $x \le \frac{1}{2}$ and $\rho(x, 0) = 1.0$ for $x > \frac{1}{2}$, while $u(x, 0) = 0$ and $p(x, 0) = 1$, $\forall x \in [0, 1]$. Figure 6 shows the numerical results for HLL and HLLC, compared to the exact solution at the output time $t = 5$ units. The mesh used has $M = 100$ cells, and the Courant number coefficient is $C_{\text{cfl}} = 0.9$. The difference between a complete (HLLC) Riemann solver and an incomplete (HLL) Riemann solver is evident.
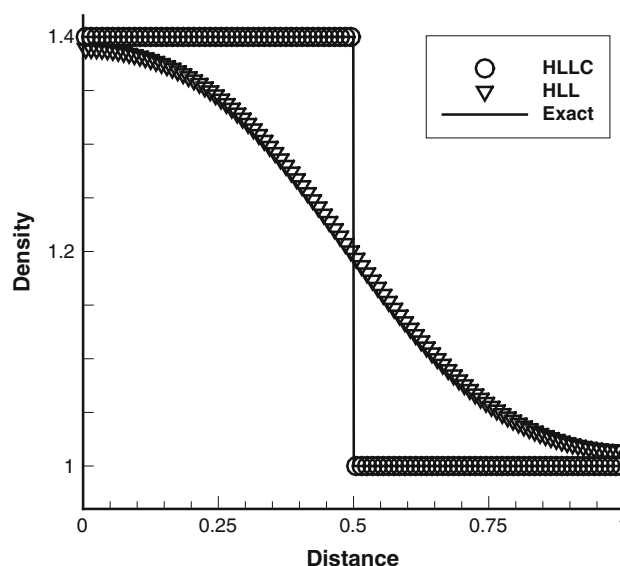
Fig. 6 Computations for an isolated stationary contact discontinuity in the 1D compressible Euler equations. Numerical results (symbols) are compared to the exact solution (full line) at the output time $t = 5$. Numerical results shown are for HLLC (circles) and HLL (triangles)

For discontinuous tangential velocity components across a stationary flow in the normal direction (x here), identical results are obtained. This observation is relevant to the accurate resolution of vortices. It is also relevant to the accurate resolution of shear layers in both inviscid and viscous flows, in which the excessive numerical dissipation of incomplete Riemann solvers, such as HLL, will mask the effect of physical viscosity. Identical results are obtained for contact discontinuities associated with species equations with discontinuous concentrations across the intermediate characteristic field. It is worth noting that in reactive flows, the accurate resolution of concentration of species is crucial in correctly enforcing ignition criteria to initiate, maintain, or stop chemical reactions.

There are many applications and extensions of the HLLC solver in the literature. This is the subject of the next section.

7 Developments in the last 25 years

In the last 25 years, the HLLC scheme has undergone considerable developments. These include algorithmic aspects and applications in a variety of fields of technological and scientific interest.

7.1 Summary and algorithmic developments

Recall that HLLC was first introduced to solve two classical hyperbolic systems, namely the compressible time-dependent Euler equations [3,4] and the compressible steady supersonic Euler equations [5]. The first system has *three*

distinct characteristic fields in one, two, and three space dimensions; in the two- and three-dimensional cases, the intermediate characteristic field is given by a repeated eigenvalue of multiplicity two in the 2D case and 3 in the 3D case. Therefore, the introduction of a single intermediate characteristic field, as in the 1D case, suffices to account for the multiple intermediate fields in the multidimensional case. Moreover, in the case of compressible, three-dimensional multicomponent flow with N added species advection equations, the approach is again able to represent all $N + 3$ resulting intermediate characteristic fields and the HLLC scheme remains a *complete* Riemann solver. For the two-dimensional shallow water equations, HLLC again becomes relevant, as the equations contain an intermediate characteristic field associated with the transverse velocity component [13]. See [6], where HLLC was successfully applied to solve these equations. As in the case of the Euler equations, if N species advection equations are added, the approach is again able to represent all $N + 1$ resulting intermediate characteristic fields, and hence, the HLLC scheme remains a *complete* Riemann solver for the two-dimensional shallow water equations augmented by N species advection equations. For the 1D blood flow equations, intermediate characteristic fields arise if N species advection equations are added; then, the HLLC approach is again able to represent all N resulting intermediate characteristic fields; the HLLC scheme remains a *complete* Riemann solver for these extended equations.

Note, however, that for systems with eigenstructure containing more than three distinct characteristic fields, HLLC becomes an *incomplete* Riemann solver, which tends to deteriorate the resolution of intermediate waves, a typical feature of *centred fluxes* and incomplete Riemann solvers. The obvious way to improve the HLLC approach is to modify it so as to admit the correct number of characteristic fields for the system of interest, or at least include those intermediate characteristic fields thought to be important, perhaps the slowest ones. A representative example of this situation is the system of compressible multiphase flow equations of Baer and Nunziato [31]. The 1D version of these equations contains seven distinct characteristic fields. The HLLC approach was extended in [32] to solve these equations, accounting for all characteristic fields and making HLLC a complete Riemann solver also for these equations. The approach applies also to the multidimensional case to account for all intermediate characteristic fields arising from the shear waves in the transverse direction. A similar situation arises with the magnetohydrodynamics equations (MHD); early extensions of HLLC to MHD are due to Gurski [33], Li [34], and Mignone and Bodo [35]. See also Bouchut et al. [36], Klingenberg et al. [37], and Honkkila and Janhunen [38]. A recently proposed scheme closely related to HLLC is the so-called HLLP solver put forward by Munz et al. [39]. Here, the intermediate wave in this case is a phase interface and thus the "P" in the name of the scheme. Large time step HLL and HLLC schemes were put forward by Prebeg et al. [40]. Pelanti [41] studied the HLLC solver for low-Mach number flows and preconditioning.

The basic HLLC flux, when inserted into the conservative finite volume formula (13), gives a Godunov scheme of first-order accuracy. More accurate, fully discrete or semidiscrete, methods can be constructed on the bases of HLLC, for which it becomes a building block. Note, however, that in view of Godunov's theorem [25], such constructions should be nonlinear. Straightforward TVD criteria [42] can be enforced empirically. More sophisticated nonlinear high-order schemes can be constructed enforcing ENO [43] and more often WENO procedures [44–48]. HLLC has also been used in the framework of discontinuous Galerkin finite element methods. See, for example, the work of van der Vegt and collaborators [49,50], Luo et al. [51], Wang and Mavriplis [52], and Qiu et al. [53]. Methodological developments for weakly hyperbolic systems are also reported by Capdeville [54]. Harris et al. [55] report results for the high-order spectral volume method on unstructured grids. See also [56]. Improvements to HLLC have been proposed in [57], where a cure for numerical shock instabilities has been proposed. A multidimensional version of the HLLC scheme has been put forward by Balsara et al. [58]. We also recall the improved version of HLL proposed in [11], called HLLEM Riemann solver, for which a multidimensional extension has also been recently proposed by Dumbser and Balsara [12].

7.2 Applications

In addition to algorithmic extensions of HLLC, there have been numerous applications reported in the literature. Some of these have been straightforward applications of the original scheme, as reviewed here, to challenging industrial and scientific problems. Other works have also involved algorithmic extensions, such as addition of more intermediate characteristic fields.

Geophysical and environmental problems An early environmental application of HLLC was to solve the two-dimensional shallow water equations to study dam-break problems, by Fraccarollo and Toro [6]. Ambati and Bokhove applied the HLLC scheme in the frame of space–time discontinuous Galerkin finite element methods to the rotating shallow water equations over varying topography [59]. Castro et al. [60] extended the scheme to solve a hyperbolic system in non-conservative form associated with turbidity currents with sediment transport. Hosseinzadeh et al. [61] applied HLLC for studying dam failure and overtopping. Ziaeddini et al. [62] applied HLLC to the numerical simulation of tidal waves over a wavy bed.

Fluid dynamics in industrial problems and technology Batten et al. [8] reported an early application of the HLLC scheme to the simulation of turbulent flows. Wells et al. [63] applied HLLC to schemes in the arbitrary Lagrangian–Eulerian (ALE) framework, while Nemec and Aftosmis [64] applied the scheme to Cartesian grids (cut cells) to solve problems involving very complex geometries. Ball and East [65] used HLLC for studying shock wave attenuation procedures. See also Navarro et al. [66], who applied the HLLC solver to hypersonic flow. Berthon et al. [67] applied the HLLC method to study a model of radiative transfer in two space dimensions; see also [68]. Gavrilyuk et al. [69] applied HLLC to study compressible elastic materials.

Ohwada et al. [70] report a novel application to compressible flows; White et al. [71] applied the HLLC scheme to flow analysis of high-speed vehicles. Pantano et al. [72] applied the scheme to compressible van der Waals supercritical fluid flows. Daude et al. [73] applied the scheme to investigate water hammer and vaporous cavitation. Examples of the more recent applications of HLLC to compressible fluid dynamics and related fields are reported in [74–86]. HLLC has also been applied to study unsteady flows and turbulence. Recent examples include [87–95].

Applications of HLLC to compressible multiphase flow have recently been reported in [96]. Saurel and Pantano [97] have reported an application of HLLC to diffused-interface capturing methods for compressible two-phase flows. See also the related works [98–102]. In biomedicine, HLLC has also been applied, for example, to the modelling of blast wave interaction with a human body and assessment of traumatic brain injury [103].

Stellar astrophysics and cosmology Early applications of the HLLC scheme concerned the magnetohydrodynamics equations. These include Gurski [33], Li [34], Mignone and Bodo [35], Bouchut et al. [36], Klingenberg et al. [37], and Honkkila and Janhunen [38]. The following are some of the more recent applications of HLLC in stellar astrophysics and cosmology: [104–122].

8 Conclusions

The HLLC extension for the HLL Riemann solver has been reviewed. HLLC restores the missing intermediate wave in the *two-wave model* HLL solver. In this way, HLLC is complete for the Euler equations, while HLL is incomplete. We have also applied the HLLC to the augmented 1D shallow water equations and note that for the two-dimensional shallow water equations the procedure for the augmented 1D case is entirely applicable to the 2D case. We have also applied here the HLLC to the augmented 1D arterial

blood flow equations. For the three-dimensional compressible Euler equations, the procedure for the 1D case is entirely applicable, as the eigenvalue $\lambda = u$ in the normal direction has multiplicity three. For the 3D multicomponent flow Euler equations with N species, again the same procedure is applicable, since the eigenvalue $\lambda = u$ has multiplicity $N + 3$. However, for systems with eigenstructure containing more than three distinct characteristic fields, the HLLC becomes *incomplete*, tending to behave like HLL for the one-dimensional Euler equations. The incomplete character of a Riemann solver affects the resolution of intermediate waves, particularly when these move slowly relative to the mesh. Therefore, the obvious way of improving the HLLC approach is to admit the correct number of characteristic fields for the system of interest. Works along these lines include [32,33,36,123], to name but a few.

In the last 25 years, we have seen many extensions of the HLLC method as well as very ambitious applications to most diverse fields of scientific applications. The author hopes that this review will contribute to shed light on both the origins of the HLLC Riemann solver and the approach to construct the HLLC flux for various hyperbolic systems. I note that there are published works, including textbooks, in which these historical aspects, as well as the description of the methods, are unclear, confusing, and even incorrect. Finally, I note that the reader is encouraged to write directly to the author to request a (free) copy of the library *NUMERICA*, which includes FORTRAN source codes for the HLLC scheme as applied to the multidimensional shallow water equations and the Euler equations of gas dynamics.

References

1. Harten, A., Lax, P.D., van Leer, B.: On upstream differencing and Godunov-type schemes for hyperbolic conservation laws. SIAM Rev. **25**(1), 35–61 (1983). https://doi.org/10.1137/1025002

2. Toro, E.F.: The weighted average flux method applied to the Euler equations. Philos. Trans. R. Soc. Lond. Ser. A Phys. Sci. Eng. **A341**, 499–530 (1992). https://doi.org/10.1098/rsta.1992.0113

3. Toro, E.F., Spruce, M., Speares, W.: Restoration of the contact surface in the HLL–Riemann solver. Technical Report CoA—9204, Department of Aerospace Science, College of Aeronautics, Cranfield Institute of Technology, UK (1992)

4. Toro, E.F., Spruce, M., Speares, W.: Restoration of the contact surface in the HLL-Riemann solver. Shock Waves **4**, 25–34 (1994). https://doi.org/10.1007/BF01414629

5. Toro, E.F., Chakraborty, A.: Development of an approximate Riemann solver for the steady supersonic Euler equations. Aeronaut. J. **98**, 325–339 (1994). https://doi.org/10.1017/S0001924000026890

6. Fraccarollo, L., Toro, E.F.: Experimental and numerical assessment of the shallow water model for two-dimensional dam-break

type problems. J. Hydraul. Res. **33**, 843–864 (1995). https://doi.org/10.1080/00221689509498555

7. Batten, P., Clarke, N., Lambert, C., Causon, D.: On the choice of wavespeeds for the HLLC Riemann solver. SIAM J. Sci. Stat. Comput. **18**, 1553–1570 (1997). https://doi.org/10.1137/S1064827593260140

8. Batten, P., Leschziner, M.A., Goldberg, U.C.: Average-state Jacobians and implicit methods for compressible viscous and turbulent flows. J. Comput. Phys. **137**, 38–78 (1997). https://doi.org/10.1006/jcph.1997.5793

9. Davis, S.F.: Simplified second-order Godunov-type methods. SIAM J. Sci. Stat. Comput. **9**, 445–473 (1988). https://doi.org/10.1137/0909030

10. Einfeldt, B.: On Godunov-type methods for gas dynamics. SIAM J. Numer. Anal. **25**(2), 294–318 (1988). https://doi.org/10.1137/0725021

11. Einfeldt, B., Munz, C.D., Roe, P.L., Sjögreen, B.: On Godunov-type methods near low densities. J. Comput. Phys. **92**, 273–295 (1991). https://doi.org/10.1016/0021-9991(91)90211-3

12. Dumbser, M., Balsara, D.: A new efficient formulation of the HLLEM Riemann solver for general conservative and non-conservative hyperbolic systems. J. Comput. Phys. **304**, 275–319 (2016). https://doi.org/10.1016/j.jcp.2015.10.014

13. Toro, E.F.: Shock-Capturing Methods for Free-Surface Shallow Flows. Wiley, Chichester (2001)

14. Toro, E.F.: Brain venous haemodynamics, neurological diseases and mathematical modelling. A review. Appl. Math. Comput. **272**, 542–579 (2016). https://doi.org/10.1016/j.amc.2015.06.066

15. Toro, E.F.: Riemann Solvers and Numerical Methods for Fluid Dynamics, 3rd edn. Springer, Berlin (2009). https://doi.org/10.1007/b79761

16. Liou, M.S., Steffen, C.J.: A new flux splitting scheme. J. Comput. Phys. **107**, 23–39 (1993). https://doi.org/10.1006/jcph.1993.1122

17. Toro, E.F., Vázquez-Cendón, M.E.: Flux splitting schemes for the Euler equations. Comput. Fluids **70**, 1–12 (2012). https://doi.org/10.1016/j.compfluid.2012.08.023

18. Toro, E.F., Castro, C.E., Lee, B.J.: A novel numerical flux for the 3D Euler equations with general equation of state. J. Comput. Phys. **303**, 80–94 (2015). https://doi.org/10.1016/j.jcp.2015.09.037

19. Tokareva, S.A., Toro, E.F.: A flux splitting method for the Baer–Nunziato equations of compressible two-phase flow. J. Comput. Phys. **323**, 45–74 (2016). https://doi.org/10.1016/j.jcp.2016.07.019

20. Balsara, D.S., Montecinos, G.I., Toro, E.F.: Exploring various flux vector splittings for the magnetohydrodynamic system. J. Comput. Phys. **311**, 1–21 (2016). https://doi.org/10.1016/j.jcp.2016.01.029

21. Steger, J.L., Warming, R.F.: Flux vector splitting of the inviscid gasdynamic equations with applications to finite-difference methods. J. Comput. Phys. **40**, 263–293 (1981). https://doi.org/10.1016/0021-9991(81)90210-2

22. van Leer, B.: Flux-vector splitting for the Euler equations. Technical Report ICASE 82–30, NASA Langley Research Center, USA (1982)

23. Zha, G.-C., Bilgen, E.: Numerical solution of Euler equations by a new flux vector splitting scheme. Int. J. Numer. Methods Fluids **17**, 115–144 (1993). https://doi.org/10.1002/fld.1650170203

24. Toro, E.F.: The Riemann problem: solvers and numerical fluxes. In: Abgrall, R., Shu, C.W. (eds.) Elsevier Handbook of Numerical Methods for Hyperbolic Problems. Chapter 2, vol. 17, pp. 19–54 (2016). https://doi.org/10.1016/bs.hna.2016.09.015

25. Godunov, S.K.: A finite difference method for the computation of discontinuous solutions of the equations of fluid dynamics. Sb. Math. **47**, 357–393 (1959)

26. Toro, E.F.: Riemann problems and the WAF method for solving two-dimensional shallow water equations. Philos. Trans. R. Soc. Lond. Ser. A Phys. Sci. Eng. **A338**, 43–68 (1992). https://doi.org/10.1098/rsta.1992.0002

27. Formaggia, L., Quarteroni, A., Veneziani, A. (eds.): Cardiovascular Mathematics. Modeling and Simulation of the Circulatory System. Springer, Berlin (2009). https://doi.org/10.1007/978-88-470-1152-6

28. Müller, L.O., Toro, E.F.: A global multiscale model for the human circulation with emphasis on the venous system. Int. J. Numer. Methods Biomed. Eng. **30**(7), 681–725 (2014). https://doi.org/10.1002/cnm.2622

29. Müller, L.O., Toro, E.F.: Enhanced global mathematical model for studying cerebral venous blood flow. J. Biomech. **47**(13), 3361–3372 (2014). https://doi.org/10.1016/j.jbiomech.2014.08.005

30. Safranov, A.V.: Difference method for gasdynamical equations based on the jump conditions. Math. Modell. **20**, 76–84 (2008). **(in Russian)**

31. Baer, M.R., Nunziato, J.W.: A Two-phase mixture theory for the deflagration-to-detonation transition (DDT) in reactive granular materials. J. Multiphase Flow **12**, 861–889 (1986). https://doi.org/10.1016/0301-9322(86)90033-9

32. Tokareva, S.A., Toro, E.F.: HLLC-type Riemann solver for the Baer–Nunziato equations of compressible two-phase flow. J. Comput. Phys. **229**, 3573–3604 (2010). https://doi.org/10.1016/j.jcp.2010.01.016

33. Gurski, K.F.: An HLLC-type approximate Riemann solver for ideal magnetohydrodynamics. SIAM J. Sci. Comput. **25**(6), 2165–2187 (2004). https://doi.org/10.1137/S1064827502407962

34. Li, S.: An HLLC Riemann solver for magneto-hydrodynamics. J. Comput. Phys. **203**(1), 344–357 (2005). https://doi.org/10.1016/j.jcp.2004.08.020

35. Mignone, A., Bodo, G.: An HLLC Riemann solver for relativistic flows - II. Magnetohydrodynamics. Mon. Not. R. Astron. Soc. **368**(3), 1040–1054 (2006). https://doi.org/10.1111/j.1365-2966.2006.10162.x

36. Bouchut, F., Klingenberg, C., Waagan, K.: A multiwave approximate Riemann solver for ideal MHD based on relaxation, I: theoretical framework. Numer. Math. **108**(1), 7–42 (2007). https://doi.org/10.1007/s00211-007-0108-8

37. Klingenberg, C., Schmidt, W., Waagan, K.: Numerical comparison of Riemann solvers for astrophysical hydrodynamics. J. Comput. Phys. **227**(1), 12–35 (2007). https://doi.org/10.1016/j.jcp.2007.07.034

38. Honkkila, V., Janhunen, P.: HLLC solver for ideal relativistic MHD. J. Comput. Phys. **223**(2), 643–656 (2007). https://doi.org/10.1016/j.jcp.2006.09.027

39. Fetcher, S., Munz, C.D., Rohde, C., Zeiler, C.: Approximate Riemann solver for compressible liquid vapor flow with phase transition and surface tension. Comput. Fluids **169**, 169–185 (2018). https://doi.org/10.1016/j.compfluid.2017.03.026

40. Prebeg, M., Flåtten, T., Müller, B.: Large time step HLL and HLLC schemes. ESAIM: M2AN (2017). https://doi.org/10.1051/m2an/2017051

41. Pelanti, M.: Wave structure similarity of the HLLC and ROE Riemann solvers: application to low Mach number preconditioning. SIAM J. Sci. Comput. **40**(3), A1836–A1859 (2018). https://doi.org/10.1137/17M1154965

42. Sweby, P.K.: High resolution schemes using flux limiters for hyperbolic conservation laws. SIAM J. Numer. Anal. **21**, 995–1011 (1984). https://doi.org/10.1137/0721062

43. Harten, A., Osher, S.: Uniformly high-order accurate nonoscillatory schemes I. SIAM J. Numer. Anal. **24**(2), 279–309 (1987). https://doi.org/10.1137/0724022

44. Jiang, G.S., Shu, C.W.: Efficient implementation of weighted ENO schemes. J. Comput. Phys. **126**, 202–228 (1996). https://doi.org/10.1006/jcph.1996.0130

45. Balsara, D., Shu, C.W.: Monotonicity preserving weighted essentially nonoscillatory schemes with increasingly high order of accuracy. J. Comput. Phys. **160**, 405–452 (2000). https://doi.org/10.1006/jcph.2000.6443

46. Titarev, V.A., Toro, E.F.: Finite-volume WENO schemes for three-dimensional conservation laws. J. Comput. Phys. **201**(1), 238–260 (2004). https://doi.org/10.1016/j.jcp.2004.05.015

47. Dumbser, M., Käser, M.: Arbitrary high order non-oscillatory finite volume schemes on unstructured meshes for linear hyperbolic systems. J. Comput. Phys. **221**(2), 693–723 (2007). https://doi.org/10.1016/j.jcp.2006.06.043

48. Dumbser, M., Käser, M., Titarev, V.A., Toro, E.F.: Quadrature-free non-oscillatory finite volume schemes on unstructured meshes for nonlinear hyperbolic systems. J. Comput. Phys. **226**(8), 204–243 (2007). https://doi.org/10.1016/j.jcp.2007.04.004

49. van der Vegt, J.J.W., van der Ven, H.: Space–time discontinuous Galerkin finite element method with dynamic grid motion for inviscid compressible flows: I. General formulation. J. Comput. Phys. **182**(2), 546–585 (2002). https://doi.org/10.1006/jcph.2002.7185

50. Pesch, L., van der Vegt, J.J.W.: A discontinuous Galerkin finite element discretization of the Euler equations for compressible and incompressible fluids. J. Comput. Phys. **227**(11), 5426–5446 (2008). https://doi.org/10.1016/j.jcp.2008.01.046

51. Luo, H., Baum, J.D., Löhner, R.: A Hermite WENO-based limiter for discontinuous Galerkin method on unstructured grids. J. Comput. Phys. **225**(1), 686–713 (2007). https://doi.org/10.1016/j.jcp.2006.12.017

52. Wang, L., Mavriplis, D.J.: Implicit solution of the unsteady Euler equations for high-order accurate discontinuous Galerkin discretizations. J. Comput. Phys. **225**(2), 1994–2015 (2007). https://doi.org/10.1016/j.jcp.2007.03.002

53. Qiu, J., Khoo, B.C., Shu, C.W.: A numerical study for the performance of the Runge–Kutta discontinuous Galerkin method based on different numerical fluxes. J. Comput. Phys. **212**(2), 540–565 (2006). https://doi.org/10.1016/j.jcp.2005.07.011

54. Capdeville, G.: Towards a compact high-order method for nonlinear hyperbolic systems, II. The Hermite-HLLC scheme. J. Comput. Phys. **227**(22), 9428–9462 (2008). https://doi.org/10.1016/j.jcp.2008.06.024

55. Harris, R., Wang, Z.J., Liu, Y.: Efficient quadrature-free high-order spectral volume method on unstructured grids: Theory and 2D. J. Comput. Phys. **227**(3), 1620–1642 (2008). https://doi.org/10.1016/j.jcp.2007.09.012

56. Li, L., Liu, X., Lou, J., Luo, H., Nishikawa, H., Ren, Y.: A discontinuous Galerkin method based on variational reconstruction for compressible flows on arbitrary grids. 2018 AIAA Aerospace Sciences Meeting, Kissimmee, Florida, AIAA Paper 2018-0831 (2018). https://doi.org/10.2514/6.2018-0831

57. Simon, S., Mandal, J.C.: A cure for numerical shock instability in HLLC Riemann solver using antidiffusion control. Comput. Fluids **174**, 144–166 (2018). https://doi.org/10.1016/j.compfluid.2018.07.001

58. Balsara, D.S., Dumbser, M., Abgrall, R.: Multidimensional HLLC Riemann solver for unstructured meshes—With application to Euler and MHD flows. J. Comput. Phys. **261**, 172–208 (2014). https://doi.org/10.1016/j.jcp.2013.12.029

59. Ambati, V.R., Bokhove, O.: Space–time discontinuous Galerkin discretization of rotating shallow water equations. J. Comput. Phys. **225**(2), 1233–1261 (2007). https://doi.org/10.1016/j.jcp.2007.01.036

60. Castro Díaz, M.J., Fernandez-Nieto, E.D., Morales de Luna, T., Narbona-Reina, G., Parés, C.: A HLLC scheme for non-conservative hyperbolic problems. Application to turbidity currents with sediment transport. ESAIM Math. Modell. Numer. Anal. **47**(2), 1–32 (2013). https://doi.org/10.1051/m2an/2012017

61. Hosseinzadeh-Tabrizi, S.A., Ghaeini-Hessaroeyeh, M.: Application of bed load formulations for dam failure and overtopping. Civ. Eng. J. **3**(10), 997–1007 (2017). https://doi.org/10.28991/cej-030932

62. Ziaeddini-Dashtkhaki, M., Ghaeini-Hessaroeyeh, M.: Numerical simulation of tidal wave over wavy bed. J. Coast. Mar. Eng. **1**(1), 7–12 (2018)

63. Wells, B.V., Baines, M.J., Glaister, P.: Generation of arbitrary Lagrangian–Eulerian (ALE) velocities, based on monitor functions, for the solution of compressible fluid equations. Int. J. Numer. Methods Fluids **47**, 1375–1381 (2005). https://doi.org/10.1002/fld.915

64. Nemec, A., Aftosmis, M.J.: Adjoint sensitivity computations for an embedded-boundary Cartesian mesh method. J. Comput. Phys. **227**(4), 2724–2742 (2008). https://doi.org/10.1016/j.jcp.2007.11.018

65. Ball, G.J., East, R.A.: Shock and blast attenuation by aqueous foam barriers: influences of barrier geometry. Shock Waves **9**(1), 37–47 (1999). https://doi.org/10.1007/s001930050137

66. Navarro-Martinez, S., Tutty, O.R.: Numerical simulation of Görtler vortices in hypersonic compression ramps. Comput. Fluids **34**(2), 225–247 (2005). https://doi.org/10.1016/j.compfluid.2004.05.002

67. Berthon, C., Charrier, P., Dubroca, B.: An HLLC scheme to solve The M_1 model of radiative transfer in two space dimensions. J. Sci. Comput. **31**(3), 347–389 (2007). https://doi.org/10.1007/s10915-006-9108-6

68. Berthon, C., Coquel, F., Hérard, J.M., Uhlmann, M.: An approximate solution of the Riemann problem for a realisable second-moment turbulent closure. Shock Waves **11**(4), 245–269 (2002). https://doi.org/10.1007/s001930100109

69. Gavrilyuk, S.L., Favrie, N., Saurel, R.: Modelling wave dynamics of compressible elastic materials. J. Comput. Phys. **227**(5), 2941–2969 (2007). https://doi.org/10.1016/j.jcp.2007.11.030

70. Ohwada, T., Shibata, Y., Kato, T., Nakamura, T.: A simple, robust and efficient high-order accurate shock-capturing scheme for compressible flows: Towards minimalism. J. Comput. Phys. **362**, 131–162 (2018). https://doi.org/10.1016/j.jcp.2018.02.019

71. White, J.A., Baurle, R.A., Passe, B.J., Spiegel, S.C., Nishikawa, H.: Geometrically flexible and efficient flow analysis of high speed vehicles via domain decomposition, Part 1: unstructured-grid solver for high speed flows. Conference: JANNAF 48th Combustion 36th Airbreathing Propulsion, pp. 1–22 (2017)

72. Pantano, C., Saurel, R., Schmitt, T.: An oscillation free shock-capturing method for compressible van der Waals supercritical fluid flows. J. Comput. Phys. **335**, 780–811 (2017). https://doi.org/10.1016/j.jcp.2017.01.057

73. Daude, F., Tijsseling, A.S., Galon, P.: Numerical investigations of water-hammer with column-separation induced by vaporous cavitation using a one-dimensional finite-volume approach. J. Fluids Struct. **83**, 91–118 (2018). https://doi.org/10.1016/j.jfluidstructs.2018.08.014

74. Sousa, J., Paniagua, G., Morata, E.C.: Thermodynamic analysis of a gas turbine engine with a rotating detonation combustor. Appl. Energy **195**, 247–256 (2017). https://doi.org/10.1016/j.apenergy.2017.03.045

75. Knudsen, E., Doran, E.M., Mittal, V., Meng, J., Spurlock, W.: Compressible Eulerian needle-to-target large eddy simulations of a diesel fuel injector. Proc. Combust. Inst. **36**(2), 2459–2466 (2017). https://doi.org/10.1016/j.proci.2016.08.016

76. Garrick, D.P., Owkes, M., Regele, J.D.: A finite-volume HLLC-based scheme for compressible interfacial flows with surface

tension. J. Comput. Phys. **339**, 46–67 (2017). https://doi.org/10.1016/j.jcp.2017.03.007

77. Fujisawa, K., Yamagata, T., Fujisawa, N.: Damping effect on impact pressure from liquid droplet impingement on wet wall. Ann. Nucl. Energy **121**, 260–268 (2018). https://doi.org/10.1016/j.anucene.2018.07.008

78. Godunov, S.K., Klyuchinskiy, D.V., Safronov, A.V., Fortova, S.V., Shepelev, V.V.: Experimental study of numerical methods for the solution of gas dynamics problems with shock waves. J. Phys.: Conf. Ser. **946**, 012048 (2018). https://doi.org/10.1088/1742-6596/946/1/012048

79. Godunov, S.K., Klyuchinskii, D.V., Fortova, S.V., Shepelev, V.V.: Experimental studies of difference gas dynamics models with shock waves. Comput. Math. Math. Phys. **58**(8), 1201–1216 (2018). https://doi.org/10.1134/S0965542518080067

80. Varma, D., Chandrashekar, P.: A second-order well-balanced finite volume scheme for Euler equations with gravity. Comput. Fluids **181**, 292–313 (2019). https://doi.org/10.1016/j.compfluid.2019.02.003

81. Wilkinson, S.D., Braithwaite, M., Nikiforakis, N., Michael, L.: A complete equation of state for non-ideal condensed phase explosives. J. Appl. Phys. **122**(22), 225112 (2017). https://doi.org/10.1063/1.5006901

82. Goncalves, E., Hoarau, Y., Zeidan, D.: Simulation of shock-induced bubble collapse using a four-equation model. Shock Waves **29**(1), 221–234 (2018). https://doi.org/10.1007/s00193-018-0809-1

83. Thornber, B., Griffond, J., Poujade, O., Attal, N., Varshochi, H., Bigdelou, P., Ramaprabhu, P., Olson, B., Greenough, J., Zhou, Y., et al.: Late-time growth rate, mixing, and anisotropy in the multimode narrowband Richtmyer–Meshkov instability: The θ-group collaboration. Phys. Fluids **29**(10), 105107 (2017). https://doi.org/10.1063/1.4993464

84. Joncquieres, V., Pechereau, F., Alvarez Laguna, A., Bourdon, A., Vermorel, O., Cuenot, B.: A 10-moment fluid numerical solver of plasma with sheaths in a Hall Effect Thruster. 2018 Joint Propulsion Conference, Cincinnati, Ohio, AIAA Paper 2018-4905 (2018). https://doi.org/10.2514/6.2018-4905

85. Wermelinger, F., Rasthofer, U., Hadjidoukas, P.E., Koumoutsakos, P.: Petascale simulations of compressible flows with interfaces. J. Comput. Sci. **26**, 217–225 (2018). https://doi.org/10.1016/j.jocs.2018.01.008

86. Sangam, A.: An HLLC scheme for ten-moments approximation coupled with magnetic field. Int. J. Comput. Sci. Math. **2**(1/2), 73–109 (2008). https://doi.org/10.1504/IJCSM.2008.019724

87. Singh, A.P.: A framework to improve turbulence models using full-field inversion and machine learning. PhD Thesis, Aerospace Engineering, The University of Michigan, USA (2018)

88. Ritos, K., Kokkinakis, I.W., Drikakis, D., Spottswood, S.M.: Implicit large eddy simulation of acoustic loading in supersonic turbulent boundary layers. Phys. Fluids **29**(4), 046101 (2017). https://doi.org/10.1063/1.4979965

89. Walchli, B., Thornber, B.: Reynolds number effects on the single-mode Richtmyer–Meshkov instability. Phys. Rev. E **95**(1), 013104 (2017). https://doi.org/10.1103/PhysRevE.95.013104

90. Islam, A., Thornber, B.: A high-order hybrid turbulence model with implicit large-eddy simulation. Comput. Fluids **167**, 292–312 (2018). https://doi.org/10.1016/j.compfluid.2018.03.031

91. Park, M.A., Barral, N., Ibanez, ., Kamenetskiy, D.S., Krakos, J.A., Michal, T.R., Loseille, A.: Unstructured grid adaptation and solver technology for turbulent flows. 2018 AIAA Aerospace Sciences Meeting, Kissimmee, Florida, AIAA Paper 2018-1103 (2018). https://doi.org/10.2514/6.2018-1103

92. Pan, L., Padoan, P., Nordlund, Å.: Detailed balance and exact results for density fluctuations in supersonic turbulence. Astrophys. J. Lett. **866**, L17 (2018). https://doi.org/10.3847/2041-8213/aae57c

93. Hahn, M., Drikakis, D.: Large eddy simulation of compressible turbulence using high-resolution methods. Int. J. Numer. Methods Fluids **47**, 971–977 (2005). https://doi.org/10.1002/fld.882

94. Kalveit, M., Drikakis, D.: Coupling strategies for hybrid molecular—continuum simulation methods. Proc. IMechE Part C J. Mech. Eng. Sci. **222**, 797–806 (2008). https://doi.org/10.1243/09544062JMES716

95. Hahn, M., Drikakis, D.: Implicit large-eddy simulation of swept wing flow using high-resolution methods. AIAA J. **47**, 618–629 (2009). https://doi.org/10.2514/1.37806

96. Pelanti, M.: Low Mach number preconditioning techniques for Roe-type and HLLC-type methods for a two-phase compressible flow model. Appl. Math. Comput. **310**, 112–133 (2017). https://doi.org/10.1016/j.amc.2017.04.014

97. Saurel, R., Pantano, C.: Diffuse-interface capturing methods for compressible two-phase flows. Annu. Rev. Fluid Mech. **50**, 105–130 (2018). https://doi.org/10.1146/annurev-fluid-122316-050109

98. Pan, S., Han, L., Hu, X., Adams, N.: A conservative sharp-interface method for compressible multi-material flows. J. Comput. Phys. **371**, 870–895 (2018). https://doi.org/10.1016/j.jcp.2018.02.007

99. Daude, F., Galon, P.: A finite-volume approach for compressible single- and two-phase flows in flexible pipelines with fluid–structure interaction. J. Comput. Phys. **362**, 375–408 (2018). https://doi.org/10.1016/j.jcp.2018.01.055

100. De Lorenzo, M.: Modelling and numerical simulation of metastable two-phase flows. PhD Thesis, Université Paris-Saclay (2018)

101. De Lorenzo, M., Pelanti, M., Lafon, P.: HLLC-type and path-conservative schemes for a single-velocity six-equation two-phase flow model: A comparative study. Appl. Math. Comput. **333**, 95–117 (2018). https://doi.org/10.1016/j.amc.2018.03.092

102. Zheng, H.W., Shu, C., Chew, Y.T.: An object-oriented and quadrilateral-mesh based solution adaptive algorithm for compressible multi-fluid flows. J. Comput. Phys. **227**(14), 6895–6921 (2008). https://doi.org/10.1016/j.jcp.2008.03.037

103. Tan, X.G., Przekwas, A.J., Gupta, R.K.: Computational modeling of blast wave interaction with a human body and assessment of traumatic brain injury. Shock Waves **27**, 889–904 (2017). https://doi.org/10.1007/s00193-017-0740-x

104. Paxton, B., Schwab, J., Bauer, E.B., Bildsten, L., Blinnikov, S., Paul Duffell, R., Farmer, J.A., Goldberg, P.M., Sorokina, E., et al.: Modules for experiments in stellar astrophysics (MESA): Convective boundaries, element diffusion, and massive star explosions. Astrophys. J. Suppl. Ser. **234**(2), 34 (2018). https://doi.org/10.3847/1538-4365/aaa5a8

105. Schneider, E.E., Robertson, B.E.: Hydrodynamical coupling of mass and momentum in multiphase galactic winds. Astrophys. J. **834**(2), 144 (2017). https://doi.org/10.3847/1538-4357/834/2/144

106. Trebitsch, M., Blaizot, J., Rosdahl, J., Devriendt, J., Slyz, A.: Fluctuating feedback-regulated escape fraction of ionizing radiation in low-mass, high-redshift galaxies. Mon. Not. R. Astron. Soc. **470**(1), 224–239 (2017). https://doi.org/10.1093/mnras/stx1060

107. Padnos, D., Mandelker, N., Birnboim, Y., Dekel, A., Krumholz, M.R., Steinberg, E.: Instability of supersonic cold streams feeding galaxies—II. Non-linear evolution of surface and body modes of Kelvin–Helmholtz instability. Mon. Not. R. Astron. Soc. **477**(3), 2933–2968 (2018). https://doi.org/10.1093/mnras/sty789

108. Radice, D., Burrows, A., Vartanyan, D., Skinner, M.A., Dolence, J.C.: Electron-capture and low-mass iron-core-collapse supernovae: New neutrino-radiation–hydrodynamics simulations.

Astrophys. J. **850**(1), 43 (2017). https://doi.org/10.3847/1538-4357/aa92c5

109. Ohlmann, S.T., Röpke, F.K., Pakmor, R., Springel, V.: Constructing stable 3D hydrodynamical models of giant stars. Astron. Astrophys. **599**, A5 (2017). https://doi.org/10.1051/0004-6361/201629692

110. Rosdahl, J., Katz, H., Blaizot, J., Kimm, T., Michel-Dansac, L., Garel, T., Haehnelt, M., Ocvirk, P., Teyssier, R.: The SPHINX cosmological simulations of the first billion years: the impact of binary stars on reionization. Mon. Not. R. Astron. Soc. **479**(1), 994–1016 (2018). https://doi.org/10.1093/mnras/sty1655

111. Cielo, S., Bieri, R., Volonteri, M., Wagner, A.Y., Dubois, Y.: AGN feedback compared: jets versus radiation. Mon. Not. R. Astron. Soc. **477**(1), 1336–1355 (2018). https://doi.org/10.1093/mnras/sty708

112. Bambic, C.J., Morsony, B.J., Reynolds, C.S.: Suppression of AGN-driven turbulence by magnetic fields in a magnetohydrodynamic model of the intracluster medium. Astrophys. J. **857**(2), 84 (2018). https://doi.org/10.3847/1538-4357/aab558

113. Beckmann, R.S.: From seed to supermassive: simulating the origin, evolution and impact of massive black holes. PhD Thesis, University of Oxford (2017)

114. Miranda-Aranguren, S., Aloy, M.A., Rembiasz, T.: An HLLC Riemann solver for resistive relativistic magnetohydrodynamics. Mon. Not. R. Astron. Soc. **476**(3), 3837–3860 (2018). https://doi.org/10.1093/mnras/sty419

115. Scannapieco, E., Safarzadeh, M.: Modeling star formation as a Markov process in a supersonic gravoturbulent medium. Astrophys. J. Lett. **865**(2), L14 (2018). https://doi.org/10.3847/2041-8213/aae1f9

116. Leroy, M.H.J., Keppens, R.: On the influence of environmental parameters on mixing and reconnection caused by the Kelvin–Helmholtz instability at the magnetopause. Phys. Plasmas **24**(1), 012906 (2017). https://doi.org/10.1063/1.4974758

117. Rasthofer, U., Wermelinger, F., Hadijdoukas, P., Koumoutsakos, P.: Large scale simulation of cloud cavitation collapse. Procedia Comput. Sci. **108**, 1763–1772 (2017). https://doi.org/10.1016/j.procs.2017.05.158

118. Navarro, A., Lora-Clavijo, F.D., González, G.A.: Magnus: A new resistive MHD code with heat flow terms. Astrophys. J. **844**(1), 57 (2017). https://doi.org/10.3847/1538-4357/aa7a13

119. Mignone, A.: MHD modeling: Aims, usage, scales assessed, caveats, codes. In: Torres, D. (ed.) Modelling Pulsar Wind Nebulae. Astrophysics and Space Science Library, vol. 446. Springer, Cham (2017)

120. Ryan, G.: Numerical simulations of black hole accretion. PhD Thesis, New York University (2017)

121. Suarez Noguez, T.: Understanding the distribution of gas in the Universe. PhD Thesis, UCL (University College London) (2018)

122. Harpole, A.: Multiscale modelling of neutron star oceans. PhD Thesis, University of Southampton (2018)

123. Takahiro, M., Kanya, K.: A multi-state HLL approximate Riemann solver for ideal magnetohydrodynamics. J. Comput. Phys. **208**(1), 315–344 (2005). https://doi.org/10.1016/j.jcp.2005.02.017